npj | clean water

www.nature.com/npjcleanwater

ARTICLE OPEN

Check for updates

Degradation of bisphenol A in an oxidation system constructed from Mo_2C MXene and peroxymonosulfate

Xuwen Chen[1], Fredrick Owino Gudda[1], Xiaojie Hu[1], Michael Gatheru Waigi[1] and Yanzheng Gao[1]✉

The etched Mo_2C MXene with a layered structure was characterized as an environmentally friendly catalyst in the bisphenol A (BPA) removal by advanced oxidation. 99.75% of BPA was degraded in the oxidation system constructed using Mo_2C MXene and peroxymonosulfate (PMS). The Mo_2C MXene was recyclable, with a high removal percentage (89.29%) of BPA after even four cycles. The catalysis of Mo_2C MXene on PMS was due to the Mo-deficit vacancy defects. The electron paramagnetic resonance technique and density functional theory (DFT)-based density of states calculations verified defect signals. In addition, the defective Mo_2C MXene and PMS have strong binding and electron transfer capabilities. The reactive oxygen species (ROS, including $O_2^{\bullet-}$, $^1O_2$, $SO_4^{\bullet-}$, and $^{\bullet}OH$) produced by Mo_2C MXene activates PMS, leading to BPA degradation. The condensed Fukui function predicted the active sites of the BPA molecule and found that the O1, O2, C3, C4, C6, C12, C15, and C16 sites have higher electrophilic reactivity. The C, C–C bonds, or C4/C16 sites in the isopropyl group connecting the two phenolic rings were attacked first, then further transformed BPA into non-toxic or low toxic small molecule degradation products through a series of reactions such as bond-breaking, addition, hydroxylation, and ring-opening. Moreover, the Mo_2C MXene/PMS system has strong applicability in actual water bodies. The study provides valuable insights into PMS activation by two-dimensional MXenes to remove toxic organic pollutants in an aqueous matrix.

npj Clean Water (2022)5:66 ; https://doi.org/10.1038/s41545-022-00214-w

INTRODUCTION

Bisphenol A (BPA) is an important organic chemical raw material used in the preparation of polymer materials such as epoxy resin and polycarbonate, which impact everyday life in that people are in close contact[1,2]. The US Environmental Protection Agency stipulated that the BPA flowing into the environment through various channels exceeds one million pounds annually[3]. BPA has a wide range of uses but is persistent in environmental matrices; hence it can contaminate food chains, groundwater, and oceans. The concentration of BPA in water, wastewater, food, biological liquids, consumer, and personal care products, and semi-solids were 251.00 μg L^{-1}, 384.80 μg L^{-1}, 937.49 μg kg^{-1}, 208.55 μg L^{-1}, 3590.00 μg g^{-1}, and 154820.00 μg g^{-1}, respectively[4]. In surface water and groundwater of Europe and America, the concentrations range from 0.001 to 100 mg m^{-3} [5]. In Ondo State, southwestern Nigeria, BPA concentrations were 0.41–5.19 μg L^{-1} in river water, 0.64–10.60 μg kg^{-1} in river sediments, and 0.63–0.68 μg L^{-1} in well water[6]. Also, BPA has endocrine-disrupting effects on aquatic wildlife and humans, with its acute toxicity in mammals valued at 6.50 g kg^{-1} [7,8]. BPA was detected in the urine of approximately 95% of adults in the USA and Asia[4]. And the maximum daily intake in adults was as high as 11.00 μg kg^{-1}, which was much higher than the average (30.76 ng kg^{-1}). The effects of BPA in humans include cardiovascular problems, reproductive effects, breast development problems, obesity, hormone-related cancers such as breast or prostate cancer, etc.[9]. Attention has focused on removing BPA in water, with numerous proposed technologies, such as physical adsorption, chemical adsorption or/and degradation, and biotransformation[10]. Among them, the chemical oxidation method was widely used because of its fast effect and high rate, such as TiO_2, $MnFe_2O_4$ modified g-C_3N_4/diatomite photocatalytic activation of peroxymonosulfate (PMS)[11–13]. However, the current oxidation methods also have some shortcomings, for example, requiring additional light sources; the cost of preparing composite catalysts is high and the process is complicated; the active components are easily changed and are not conducive to recycling. It is an urgent task to find a catalytic oxidation system that has a low cost of catalyst preparation and maintains a high-efficiency catalytic effect.

The advanced oxidation process based on $SO_4^{\bullet-}$ ($SO_4^{\bullet-}$-AOPs) has always received extensive attention owing to its efficient reactivity, wide operating range, good stability, and relatively low cost in detoxifying dangerous pollutants[14]. It is used to mineralize many structurally stable organic compounds or/and convert them into low-toxic and low-hazard byproducts. The peroxides such as peroxydisulfate (PDS) or PMS are activated to generate $SO_4^{\bullet-}$, and other strong oxidizing agents ($^{\bullet}OH$) and weak oxidizing agents ($O_2^{\bullet-}$ and $^1O_2$). $SO_4^{\bullet-}$ has a stronger oxidation ability (2.5–3.1 V), a long half-life ($T_{1/2} = 30–40$ s), a widely applicable pH range (3–9), and a higher selectivity than $^{\bullet}OH$ (1.8–2.7 V, $T_{1/2} = 20$ ns, pH 2–4)[15–17]. There are many ways to activate peroxides, including light[10], heat[18], bases[19], and transition metals[20–22]. In recent years, the use of solid catalysts to activate peroxides has received particular interest because of their stability and reusability.

The MXene materials are shaped like a potato chip and have a two-dimensional (2D) nanostructure. Those can be produced by etching the A layer in MAX (M: transition metal, A: IIIA/IVA group element, X: C/N)[23,24]. Mo_2C MXene material is a transition metal carbide. MXene materials have a layered or sheet structure and unique advantages, such as a large specific surface area, surface functional group design, and considerably coordinated unsaturated external atoms[25–27]. These characteristics make it possible to use MXenes alone or in combination with other materials, such as

[1]Institute of Organic Contaminant Control and Soil Remediation, College of Resources and Environmental Sciences, Nanjing Agricultural University, Nanjing 210095, China. ✉email: gaoyanzheng@njau.edu.cn

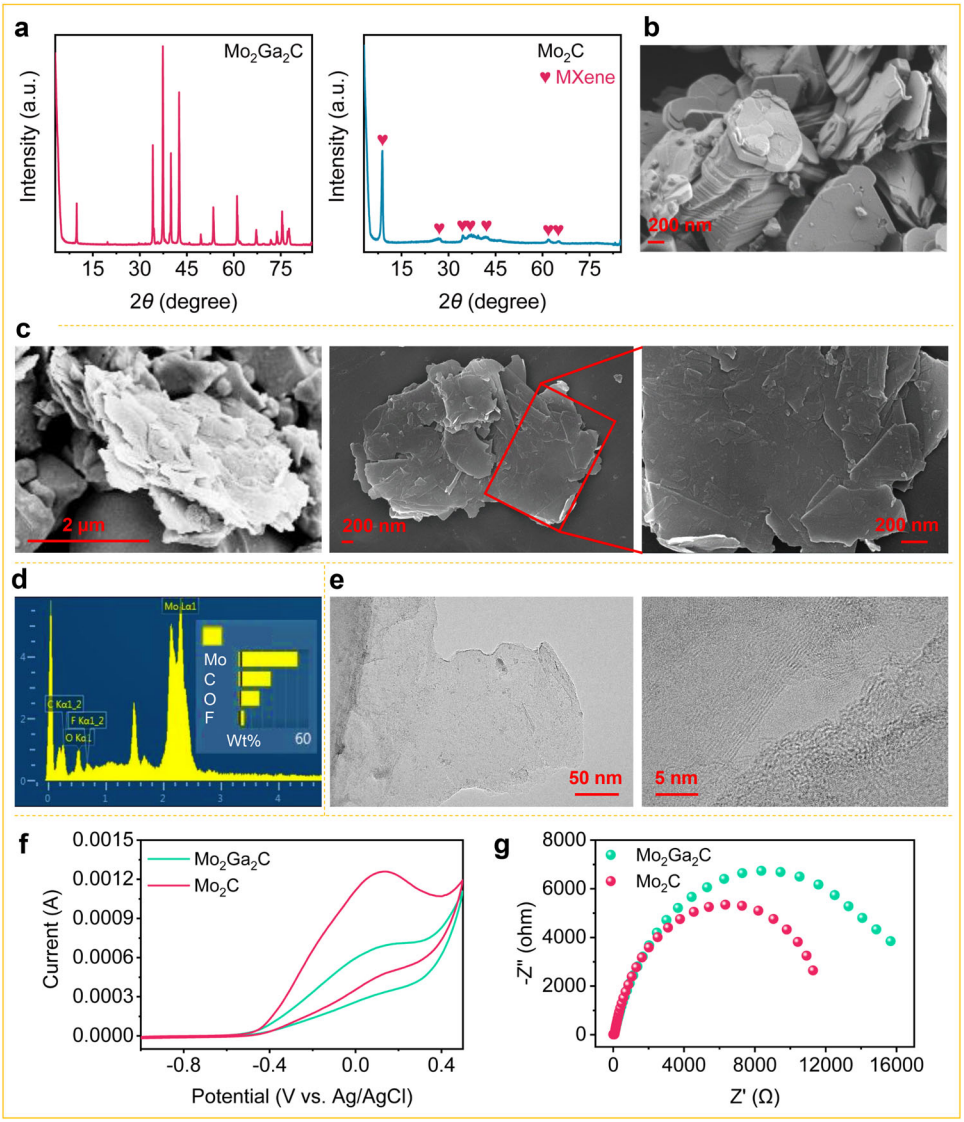

Fig. 1 Phase and morphology analysis. a Morphological analysis of Mo_2Ga_2C and Mo_2C MXene by X-ray diffraction (XRD). **b** Scanning electron microscopy (SEM) image of Mo_2Ga_2C. **c** SEM images of Mo_2C MXene. **d** SEM-EDS of Mo_2C MXene. **e** Transmission electron microscopy (TEM) images of Mo_2C MXene. **f** Cyclic voltammograms of Mo_2Ga_2C and Mo_2C MXene. **g** Nyquist plots of Mo_2Ga_2C and Mo_2C MXene.

MOFs, to prepare more advantageous composites in some fields[28]. Like the reported MOFs, MXene materials can also enhance their related application mechanisms through their own rational design, including the introduction of functional ligands, as well as structural and energy band regulation[29]. In addition, MXene materials generally have single-atom vacancy defects, which would provide a new mechanism for its application. It shows many unique characteristics and promising applications in the field of electronics. Some MXene-based materials can remove organic and inorganic contaminants to purify water and remediate polluted environments[30]. However, the research of Mo_2C MXene in catalysis is mainly the hydrogen evolution reaction[31,32]. The study of Mo_2C MXene as a peroxides activator has not been reported yet. In this work, we try to use the Mo_2C MXene material as the activator of PMS to degrade toxic organic pollutants oxidatively.

In this study, we utilized Mo_2C MXene and PMS to build an advanced catalytic oxidation system generating reactive oxygen species (ROS). BPA was used as a typical contaminant to examine the performance of the system. This work has the following objectives: (a) Morphology, phase, and mass transfer resistance were analyzed to characterize Mo_2C MXene; (b) the batch experiments were investigated to explore the activation efficiency of Mo_2C MXene on PMS and the degradation effect of Mo_2C MXene/PMS system on BPA and evaluate the stability and recyclability of Mo_2C MXene; (c) the ROS, the defect sites, and calculation of the binding capacity between defective Mo_2C/non-defective Mo_2C and PMS were analyzed to elucidate the catalytic mechanism; (d) the transformation products were measured, combined with condensed Fukui function calculation, to clarify the transformation pathways of BPA.

RESULTS AND DISCUSSION

Characteristics of Mo_2C MXene

The Mo_2Ga_2C sample was first etched with 40% hydrofluoric acid solution for 36 h at 50 °C to remove the Ga element as much as possible and form defects. As shown in Fig. 1a, the phase of Mo_2Ga_2C by XRD changed obviously after etching, and some diffraction peaks disappeared, especially the diffraction peak at 8.94° shifted to the left, and the peak intensity was noticeably enhanced. The peaks at 8.94°, 28.86°, 34.57°, 37.07°, 42.10°, 61.82°,

and 65.04° of 2θ are the diffraction peaks of the Mo_2C MXene, which indicated that the MXene material was successfully prepared. In Fig. 1b, c, SEM images showed that Mo_2Ga_2C was a solid block, and it is an apparent layered Mo_2C MXene structure after etching. The elemental content and morphology of Mo_2C MXene were further analyzed by SEM-EDS and TEM in Fig. 1d, e. Furthermore, single vacancy is the only point defect observed in MXene in experiments[33]. Also, according to previous studies, Mo_2C MXene is more prone to form Mo vacancy defects due to its relatively low single-vacancy formation energy (0.96 eV)[34]. Regarding this characteristic, its mechanism shall be discussed in detail.

To verify the electrochemically active surface area of the Mo_2C MXene, the CV of raw material Mo_2Ga_2C and Mo_2C MXene was measured in Fig. 1f. It was found that the Mo_2C MXene has a larger surface area, which implies that there were more active centers on its surface[35]. About the Nyquist plots of EIS (Fig. 1g), the radius of the arc shows the interface resistance of the electrode surface, and the smaller the radius, the lower the charge transfer resistance[36]. Among them, the Mo_2C MXene has a shorter radius than Mo_2Ga_2C, indicating that the Mo_2C MXene obtained after Mo_2Ga_2C etching has reduced charge transfer resistance, which not only accelerated the electron transfer in the Mo_2C MXene but also promoted the catalytic activity[37]. Those characteristics suggest that Mo_2C MXene is a possible material for activating PMS.

The performance of Mo_2C MXene for PMS activation to degrade BPA

As exhibited in Fig. 2a, single-use of Mo_2C MXene or PMS resulted in no BPA degradation, indicating that Mo_2C MXene and PMS have almost no BPA degradation effect. When the raw material Mo_2Ga_2C and PMS coexist, the removal rate of BPA was minimal (only 16.30%), which may be caused by the adsorption of BPA by Mo_2Ga_2C or the weak activation of PMS by the exposed transition metal atoms on Mo_2Ga_2C surface. This phenomenon implies that Mo_2Ga_2C has no effective activation effect on PMS. But when 0.5 g L^{-1} Mo_2C MXene and 2.0 mmol L^{-1} PMS exist simultaneously, the degradation percentage of BPA reached 99.75% within 240 min. And this reaction fitted the pseudo-first-order kinetic equation, with the rate constant being 0.0227 min^{-1}. This result indicates that Mo_2C MXene has excellent activation performance on PMS compared to other catalysts, and the production of stronger oxidizing substances led to the removal of BPA. For example, 0.5 g L^{-1} 70.00% copper oxide/halloysite nanotubes activated PMS to degrade 50.0 mg L^{-1} BPA, and the degradation percentage of BPA was less than 80.00% within 240 min[38]. Also, the Me(Ba, Ca, and Mg)SrCoO were used to catalytically generate $^{\bullet}OH$ and $^1O_2$ for the degradation of dye orange II; the reaction was slow and the degradation percentage was about 90.00% within 8 h[39]. The Mo_2C MXene used from two to four cycles resulted in BPA degradation percentages of 100%, 90.20%, and 89.29%, respectively (Fig. 2b). This slight inactivation may be due to the active sites being occupied by partial decomposition of organic residues, as some defective sites on the Mo_2C MXene were oxidized[15,40]. Overall, Mo_2C MXenes have good recyclability compared to some catalysts in AOPs. It has been reported that the degradation activity of the traditional iron oxide Fenton catalyst decreased from 70.00% to 10.00% in only 4 cycles[39].

The influences of Mo_2C MXene and PMS dosage, the initial solution pH, and widespread inorganic anions for BPA removal were investigated in Fig. 2c. Additionally, the reaction rate constants (Fig. 2d) were obtained by fitting the pseudo-first-order degradation kinetic curves (Supplementary Fig. 1) to get. For the concentration of Mo_2C MXene and PMS at 0.1–1.0 g L^{-1} and 0.5–5.0 mmol L^{-1}, as the dosage increased, the degradation rate of BPA increased first and then decreased. Still, the degradation percentage was close to 100% at high doses. When Mo_2C MXene and PMS were 0.5 g L^{-1} and 2.0 mmol L^{-1}, respectively, there was a great increase in k value, indicating that the two perfectly cooperate to continuously generate a large amount of ROS at this dose. Mo_2C MXene can provide more active sites and surface area, and higher PMS can offer greater contact with Mo_2C MXene[41]. However, when Mo_2C MXene was excessive, its contact with PMS was limited. And when PMS was excessive, the large amount of ROS generated instantaneously would be self-quenched, resulting in a decrease of k of BPA degradation[42,43].

BPA degradation first decreased from pH 3 to pH 7 before increasing to pH 10. BPA can be entirely degraded under acidic conditions, 92.66% under basic conditions, and 73.61% under neutral conditions. This shows that Mo_2C MXene has a wider range of applications than some Fenton-like catalysts. The biochar/iron oxide composite degraded 10 mg L^{-1} BPA at pH 3 through a Fenton-like reaction, and the degradation percentage was only 69.80% within 1000 min. And with the increase of solution pH, the degradation percentage of BPA tended to decrease[44]. The zero charge point (pH_{pzc}) of Mo_2C MXene is lower than 3 in Supplementary Fig. 2, indicating that its surface is negatively charged between pH 3–10, which is not conducive to binding with PMS molecules to produce ROS; therefore, the degradation rate of BPA gradually decreases at pH 3–7. However, there may be a process of base activation at higher pH (pH 10), which led to BPA degradation, owing to the negatively charged OH^- being easier to donate electrons than H_2O molecules[43]. This result implies that Mo_2C MXene/PMS system is effective for acidic and base conditions. Moreover, the initial unadjusted pH value of our experiment should be between 3 and 5.

Increasing the reaction temperature had a positive effect on the degradation of BPA (Supplementary Fig. 3a, b), which increased the degradation percentage and improved the reaction rate. The degradation percentage of BPA increased from 89.11% to 99.75% in 240 min from 15 °C to 25 °C, and further increased to 35 °C, BPA was completely degraded within 100 min. This was mainly because temperature accelerated the movement of molecules, which was favorable for ROS production and the interaction between ROS and pollutants, and high temperature may also contribute to the activation of PMS[45]. In addition, we calculated the activation energy using the Arrhenius equation (Supplementary Methods; Supplementary Fig. 3c), which was 524.12 J mol^{-1}.

Other types of contamination were used to evaluate the Mo_2C MXene's application potential, including the activation efficiency of Mo_2C MXene for different kinds of oxidants and the degradation effects of oxidation systems for different types of pollutants (Supplementary Fig. 4). Both PMS and PS are peroxides, and the degradation percentage of BPA in the Mo_2C MXene/PMS system was 99.75%. However, when Mo_2C MXene activated PS, BPA can be completely degraded within 80 min. This suggests that Mo_2C MXene has good applicability to persulfate-based peroxides. In addition, the degradation efficiency of Mo_2C MXene-activated PMS to BPA, bisphenol S (BPS), benzyl butyl phthalate (BBP), and naphthalene (NAP) was also explored. These pollutants were classified as endocrine disruptors, plasticizers, and PAHs, respectively. The degradation percentages of BPA, BPS, BBP, and NAP in the Mo_2C MXene/PMS system were 99.75%, 100%, 77.42%, and 100%, respectively. This indicates that the Mo_2C MXene/PMS system may have broad-spectrum removal efficiency for environmental contaminants.

Since there are generally a large number of inorganic anions remaining in the actual wastewater, it is very meaningful to study the influence of inorganic anions on the degradation of organic matter. As shown in Fig. 2c, d, NO_3^- has a weak improving efficiency for BPA removal in the Mo_2C MXene/PMS system, and Cl^- greatly promotes the degradation rate of BPA. This was mainly due to the reaction of Cl^- with HSO_5^-, $SO_4^{\bullet-}$, and $^{\bullet}OH$ to generate active chlorine species, such as $Cl^{\bullet}$ ($E_0 = 2.4$ V), $Cl_2^{\bullet-}$, Cl_2, etc., which might synergistically degrade BPA. Also, $Cl^{\bullet}$ also can catalyze the transport reaction to increase the enhancement of

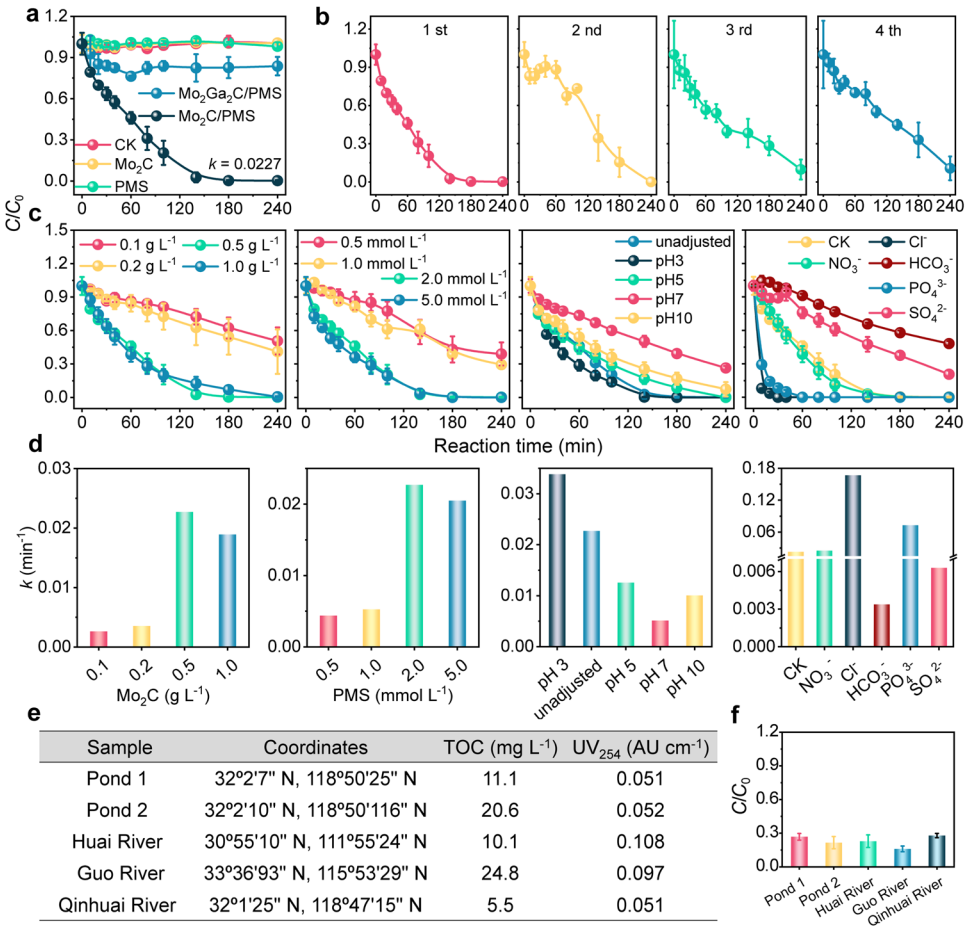

Sample	Coordinates	TOC (mg L^{-1})	UV_{254} (AU cm^{-1})
Pond 1	32°2'7" N, 118°50'25" N	11.1	0.051
Pond 2	32°2'10" N, 118°50'116" N	20.6	0.052
Huai River	30°55'10" N, 111°55'24" N	10.1	0.108
Guo River	33°36'93" N, 115°53'29" N	24.8	0.097
Qinhuai River	32°1'25" N, 118°47'15" N	5.5	0.051

Fig. 2 Mo_2C MXene activated peroxymonosulfate (PMS) for bisphenol A (BPA) degradation. a Degradation kinetics of BPA in Mo_2C MXene/PMS system. **b** Reuse efficiency of Mo_2C MXene, CK means the control treatment without Mo_2C MXene and PMS; **c** The influence of Mo_2C MXene and PMS dosage, initial solution pH, and inorganic anions on Mo_2C MXene/PMS system. **d** The reaction rate constants obtained by pseudo-first-order kinetic fitting, CK means the control treatment without inorganic anions. **e** The collection coordinates of five actual water bodies and their total organic carbon (TOC) content and UV_{254} indicators. **f** Degradation percentages of BPA in five actual water bodies. The error bars represent the standard deviation (SD). Conditions: Mo_2C MXene = 0.5 g L^{-1}, Mo_2Ga_2C = 0.5 g L^{-1}, $[PMS]_0$ = 2.0 mmol L^{-1}, [inorganic anions]$_0$ = 10.0 mmol L^{-1}, $[BPA]_0$ = 2 mg L^{-1}, pH unadjusted, and 25 °C.

$SO_4^{\bullet-}$, which was conducive to the removal of BPA[46]. Moreover, $Cl^{\bullet}$ has a higher reaction rate than $^{\bullet}OH$ for electron-rich organic pollutants[47]. This has a similar effect to Cl^- in the degradation of BPA, PAHs, and arsanilic acid by pyrrolic N-rich biochars/peroxydisulfate, polystyrene-coated persulfate polyacrylonitrile beads, and $CuFe_2O_4$/PMS, respectively[48–50]. According to Eqs. 1–4, Cl^- can be converted into active chlorine or hypochlorous substances[7,47,51,52].

$$HSO_5^- + 2Cl^- + H^+ \rightarrow Cl_2 + SO_4^{2-} + H_2O \quad (1)$$

$$SO_4^{\bullet-} + Cl^- \rightarrow Cl^{\bullet} + SO_4^{2-} \quad (2)$$

$$^{\bullet}OH + Cl^- \rightarrow HOCl^{\bullet-} \quad (3)$$

$$Cl^{\bullet} + Cl^- \rightarrow Cl_2^{\bullet-} \quad (4)$$

The active chloride ($Cl^{\bullet}$ and $Cl_2^{\bullet-}$) may attack the unsaturated bonds of pollutants to produce adsorbable organic halides that were conducive to the conversion of BPA on the surface of the Mo_2C MXene. Similar research findings have also been reported in some studies; for example, $CuFe_2O_4$/kaolinite activated PMS to degrade BPA, nZVI/carbon fiber activated PMS to degrade levofloxacin, and the degradation of Acid Orange 7 by $SO_4^{\bullet-}$-AOPs[7,53,54]. PO_4^{3-} also promotes BPA removal efficiency; this result was consistent with Khajeh et al., whereby PO_4^{3-} ions can catch the $^{\bullet}OH$ to generate $PO_4^{2\bullet}$ according to Eq. 5[55].

$$PO_4^{3-} + {}^{\bullet}OH \rightarrow PO_4^{2\cdot} + OH^- \quad (5)$$

HCO_3^- has an inhibitory effect on BPA removal in the Mo_2C MXene/PMS system, which was different from previous studies. Dong et al. believed that HCO_3^- promoted BPA removal in the system constructed by 40%-CF/K composite and PMS because it led to more active oxygen production[7]. And our research is consistent with Hammad et al., that HCO_3^- usually acts as a free radical quencher in AOPs[56]. In addition, SO_4^{2-} also greatly inhibits the BPA degradation percentage because SO_4^{2-} is the product of $SO_4^{\bullet-}$ reaction, so it would affect its conversion.

In order to explore the environmental applicability of the Mo_2C MXene/PMS system in real water, we applied it in five natural water bodies, namely Pond 1, Pond 2, Huai River, Guo River, and Qinhuai River. The sampling points of these five water bodies are shown in Fig. 2e, and the basic situation of water quality was also measured. The total organic carbon (TOC) contents were 11.10, 20.60, 10.10, 24.80, and 5.50 mg L^{-1}, respectively, for Pond 1, Pond 2, Huai River, Guo River, and Qinhuai River. UV_{254} value is the absorbance of some organic substances in the water under the ultraviolet light of 254 nm wavelength, reflecting the amount of humic macromolecular organic substances naturally present in the water. The UV_{254} value of Pond 1, Pond 2, Huai River, Guo River, and Qinhuai River were 0.05, 0.05, 0.11, 0.10, and 0.05 AU cm^{-1},

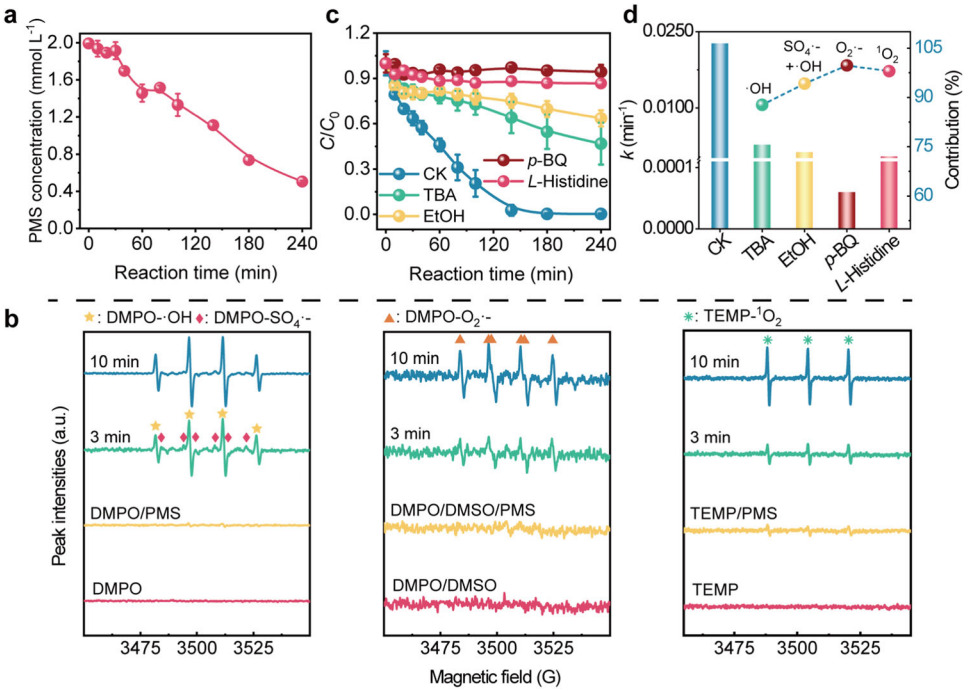

Fig. 3 Determination and contribution of reactive oxygen species (ROS). a The reducing concentrations of peroxymonosulfate (PMS). **b** Electron paramagnetic resonance (EPR) spectroscopy signal of ROS. **c** Degradation kinetics of bisphenol A (BPA) in the presence of quenchers. **d** The reaction rate constant of BPA based on pseudo-first-order kinetics fitting in the presence of quenchers, and the respective contribution of ROS to BPA degradation. The error bars represent the standard deviation (SD). Conditions: Mo_2C MXene = 0.5 g L^{-1}, $[PMS]_0$ = 2.0 mmol L^{-1}, $[DMPO]_0$ = 100 mmol L^{-1}, $[TEMP]_0$ = 30 mmol L^{-1}, $[BPA]_0$ = 2 mg L^{-1}, [TBA] = 2 mmol L^{-1}, [EtOH] = 2 mmol L^{-1}, [*p*-BQ] = 2 mmol L^{-1}, [L-Histidine] = 20 mmol L^{-1}, pH unadjusted, and 25 °C.

respectively. The degradation of BPA by the Mo_2C MXene/PMS system in Pond 1, Pond 2, Huai River, Guo River, and Qinhuai River is shown in Fig. 2f; the degradation percentages were 73.24%, 78.46%, 77.16%, 80.00%, and 72.14%, respectively. The result indicates that BPA still remains at a high degradation percentage in the real environment, and the Mo_2C MXene/PMS system has good environmental applicability.

Identification and analysis of ROS

To explore the catalytic mechanism of Mo_2C MXene on PMS, the EPR technique and quenching experiments were performed[57]. The concentration of PMS from 2.0 mmol L^{-1} decreased to 0.5 mmol L^{-1} after the reaction, which indicates that the PMS was decomposed (Fig. 3a). In Fig. 3b, there were obvious signal peaks of DMPO-$SO_4^{\bullet-}$ adduct (hyperfine coupling constants of a_N = 13.2 G, a_H = 9.7 G, a_H = 1.48 G, and a_H = 0.79 G) and DMPO-·OH adduct ($a_N = a_H$ = 14.8 G), which was mainly produced by the decomposition of PMS. The production process can be expressed by Eqs. 6 and 7[58,59]. The Mo-deficit vacancy defects on the Mo_2C MXene surface transfer an electron to the PMS, breaking the O–-O bond to generate $SO_4^{\bullet-}$, and the vacancy defects form holes. The signal of the DMPO-$SO_4^{\bullet-}$ adduct was weaker, which may be due to the rapid transformation of $SO_4^{\bullet-}$ to ·OH by nucleophilic substitution[60].

$$Mo_{2(\text{vacancy defects})}C + HSO_5^- \rightarrow Mo_{2(h+)}C + SO_4^{\bullet-} + OH^- \quad (6)$$

$$SO_4^{\bullet-} + H_2O/OH^- \rightarrow {}^{\bullet}OH + SO_4^{2-} \quad (7)$$

In addition, we have also detected the existence of DMPO-$O_2^{\bullet-}$ adduct (a_N = 14.0 G, a_H = 12.9 G) and TEMP-$^1O_2$ adduct (a_N = 16.1 G) by EPR in the Mo_2C MXene/PMS system, which was most likely to be transformed according to Eqs. 8–10[12,61]. $O_2^{\bullet-}$ was produced because O_2 contained in the water accepts an electron from Mo_2C MXene, which process has also been reported on other MXenes[62]. $O_2^{\bullet-}$ reacted with $Mo_{2(h+)}C$ to further transform into $^1O_2$, and $^1O_2$ may also be generated by PMS self-decomposition.

$$O_2 + e^- \rightarrow O_2^{\bullet-} \quad (8)$$

$$O_2^{\bullet-} + Mo_{2(h+)}C \rightarrow {}^1O_2 \quad (9)$$

$$HSO_5^- + SO_5^- \rightarrow {}^1O_2 + HSO_4^- + SO_4^{2-} \quad (10)$$

To distinguish the contribution of ROS, we conducted a quenching experiment. Among them, TBA acts on ·OH, EtOH quenches $SO_4^{\bullet-}$ and ·OH, *p*-BQ is a quencher for $O_2^{\bullet-}$, and L-Histidine for $^1O_2$. Figure 3c shows that after adding the quencher TBA, EtOH, *p*-BQ, and *L*-Histidine, the degradation percentage of BPA decreased to 53.21%, 36.43%, 5.67%, and 13.31%, respectively. The pseudo-first-order degradation kinetics of each ROS was fitted in Supplementary Fig. 5, with the reaction rate constant and the individual contribution being shown in Fig. 3d. The *k* value was significantly decreased compared with in the absence of quencher, and the corresponding ROS contribution was $O_2^{\bullet-} > {}^1O_2 >$ ·OH > $SO_4^{\bullet-}$. $SO_4^{\bullet-}$, ·OH, $O_2^{\bullet-}$, and $^1O_2$ were identified as ROS that degraded BPA to non-toxic or low-toxic small molecule degradation products or caused it to mineralize (Eq. 11).

$$BPA + SO_4^{\bullet-}/{}^{\bullet}OH/O_2^{\bullet-}/{}^1O_2 \rightarrow \text{degradation products} \quad (11)$$

Catalytic mechanism of Mo_2C MXene

To further explore the electron transfer mechanism between Mo_2C MXene and PMS, the Mo_2C MXene samples before and after the reaction were explored by XPS. As displayed in Fig. 4a, b and Supplementary Table 1, the Mo_2C MXene includes Mo, C, and O elements. The C 1*s* spectrum of Mo_2C MXene was fitted to three peaks: 284.07 eV belongs to the Mo–C bond, 284.81 eV was the C–C bond, and 288.55 eV may be contributed by oxidized C=O

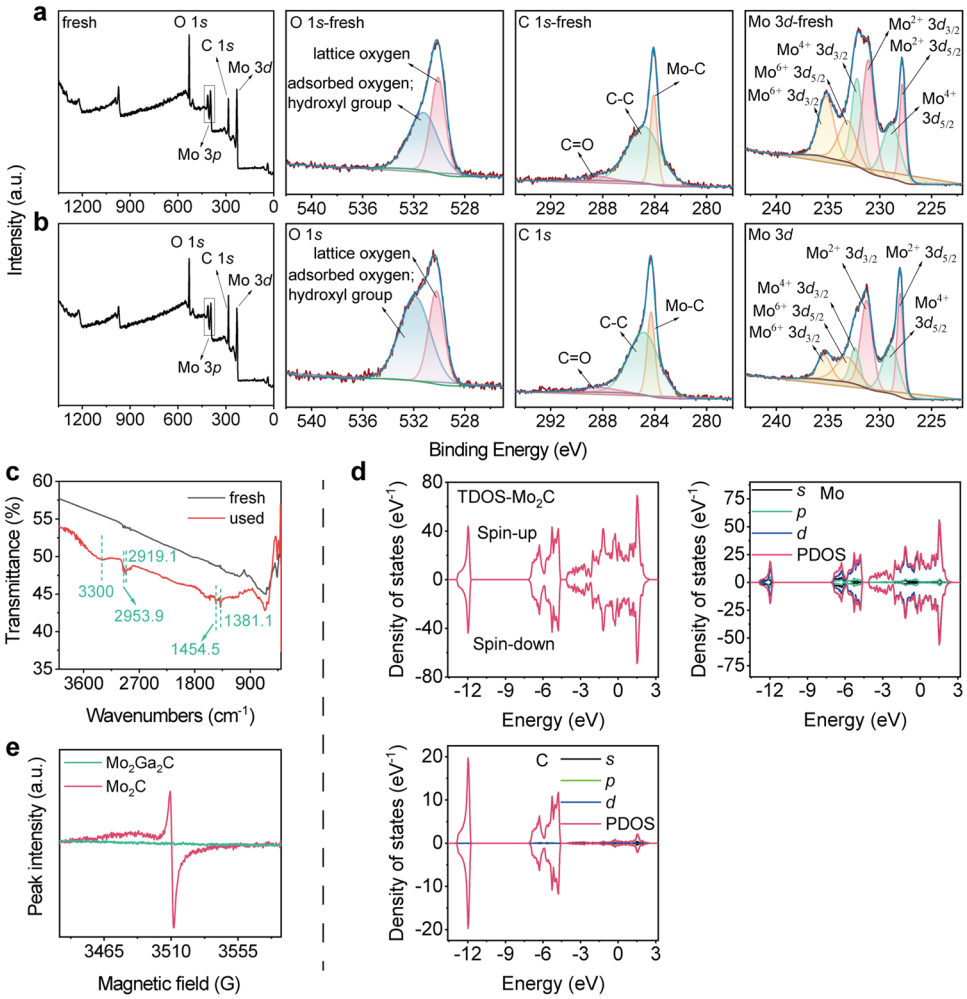

Fig. 4 Analysis of Mo-deficit vacancy defects. X-ray photoelectron spectroscopy (XPS) of the **a** fresh and **b** used Mo_2C MXene. **c** Fourier Transform Infrared (FTIR) spectrum for fresh and used Mo_2C MXene. **d** The total density of states (TDOS) and partial density of states (PDOS) of Mo_2C MXene based on density functional theory (DFT) calculation. **e** Electron paramagnetic resonance (EPR) of Mo_2Ga_2C and fresh Mo_2C MXene.

bond on Mo_2C MXene surface[26]. The O 1*s* spectrum was deconvoluted into two peaks (530.09 and 531.23 eV); they were contributed by the surface lattice oxygen in the metal–oxygen bond and adsorbed oxygen and the hydroxyl group, respectively[7,57]. The content of the adsorbed oxygen and the hydroxyl group increased from 54.96% to 64.20% after the reaction of Mo_2C MXene. The results indicate that the Mo_2C MXene surface would adsorb some oxygen-containing groups during the reaction. The high-resolution spectrum of Mo 3*d* XPS was deconvoluted into six peaks. The Mo $3d_{5/2}$ peak positions located at 227.83, 228.90, and 233.14 eV, were Mo^{2+}, Mo^{4+}, and Mo^{6+}, respectively, and the corresponding Mo $3d_{3/2}$ peak positions appear at 231.09, 232.21, and 235.19 eV[63]. Among them, Mo^{4+} and Mo^{6+} may be generated from the oxidation of the Mo_2C MXene surface[64]. In addition, we found that the content of Mo^{2+} in used Mo_2C MXene increased from 35.32% to 45.50%, while the Mo^{4+} and Mo^{6+} decreased from 34.24% and 30.44% to 30.92% and 23.57%, respectively, which implies that the Mo^{2+} in Mo_2C MXene does not transfer electrons in the catalytic process. Those results prove that the activation of PMS by Mo_2C MXene was achieved through different means other than Mo^{2+} atoms in Mo_2C MXene[65].

The functional groups from the surface of Mo_2C MXene were identified using FTIR with wavenumbers from 400 nm to 4000 nm in Fig. 4c. It was found that there were no apparent bands related to catalysis on the fresh Mo_2C MXene. Therefore, the possibility of surface functional group catalysis was excluded in the Mo_2C MXene/PMS system. Figure 4c also showed several obvious absorption peaks of bands on the used Mo_2C MXene. The two newly formed bands at 2953.9 cm and 2919.1 cm were due to C–H stretching vibration, another two bands at 1454.5 cm and 1381.1 cm were attributable to the C=O bond formed by surface oxidation, and the band at 3300 cm was O–H bond stretching vibration attached on the surface of Mo_2C MXene[66,67]. This suggests that some groups would be adsorbed on the surface after Mo_2C MXene catalyzed the PMS.

It has been reported that MXene samples (i.e., 312 phase Ti_3C_2) etched would form corresponding Ti-deficit vacancy defects, which have a strong reducing ability[68–70]. We speculated that Mo_2C MXene activation of PMS was also achieved through Mo-deficit vacancy defects on its surface. PMS first combined on the vacancy defects of Mo_2C MXene, then received electrons from unpaired spintronics on the defective site to generate ROS, while the vacancy defects transformed holes due to the loss of electrons. We measured the defect signal and analyzed the combination between defective Mo_2C/undefective Mo_2C MXene and PMS.

The density of states (DOS) of Mo_2C MXene is displayed in Fig. 4d. The energy 0 point is the Fermi level, and the *d* orbital electrons of Mo mainly contribute to the electron DOS. The electron DOS with upward and downward spin was symmetrically distributed. It further

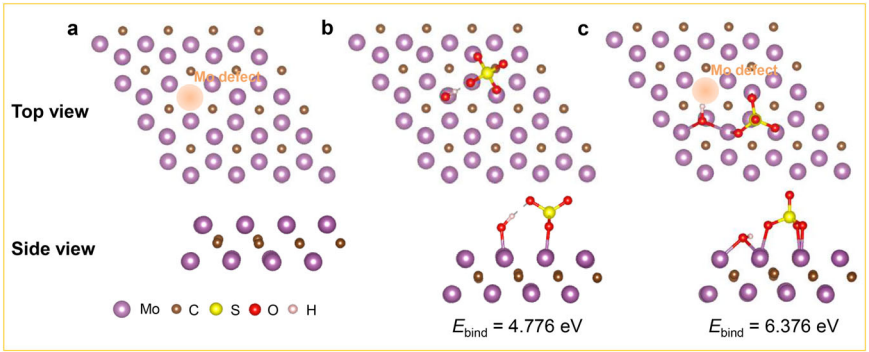

Fig. 5 The calculation of binding energy between Mo_2C MXene/defective Mo_2C MXene and peroxymonosulfate (PMS) based on density functional theory (DFT). a Structural optimization of Mo_2C MXene with Mo-deficit vacancy defects. **b** Combination between Mo_2C MXene and PMS. **c** Combination between Mo_2C MXene with Mo-deficit vacancy defects and PMS.

proved that Mo element sites are easier to form defects and may retain electrons. Moreover, there was a pronounced signal peak of Mo_2C MXene based on EPR analysis (Fig. 4e), and the g value of 2.003 is characteristic of delocalized/free electrons caused by defects in the surface of catalyst[71].

The binding energies between undefective Mo_2C MXene, defective Mo_2C MXene (there was a Mo-deficit vacancy defect in the structure), and PMS molecule (HSO_5^-) were analyzed by computational chemistry based on DFT. First, the undefective Mo_2C MXene, defective Mo_2C MXene, and HSO_5^- structural models were constructed. The energies of the three structures optimized by DFT were −465.89, −453.89, and −41.92 eV, respectively (Supplementary Fig. 6 and Fig. 5a). Then, the binding energies between undefective Mo_2C MXene/defective Mo_2C MXene and HSO_5^- were calculated using the Vienna ab-initio simulation package (VASP) with the frozen-core all-electron projector-augment-wave (PAW) method (Fig. 5b, c). It was found that the combination of HSO_5^- and undefective Mo_2C MXene does not cause the breakage of the O–O bond, but binds to the surface of the Mo_2C MXene in the form of Mo-OH-SO_3-O-Mo, and the binding energy was 4.78 eV. But after HSO_5^- was combined with the defective Mo_2C MXene, the O–O bond would be directly broken to generate OH and SO_4 groups, which were connected to the Mo atoms around the defects, and the binding energy was 6.38 eV. Eventually, the SO_4 would be converted into $SO_4^{\bullet-}$ by electron transfer. Those results indicate that the existence of defects was more favorable for the interaction between Mo_2C MXene and PMS to generate ROS for BPA degradation (Eqs. 6–11).

In addition, according to the XPS and FTIR results, the hydroxyl group content increased after Mo_2C MXene participation in the reaction. The interaction between Mo_2C MXene and the hydroxyl group was analyzed. Supplementary Fig. 7 shows the DOS of Mo_2C MXene with an adsorbed hydroxyl group. It was found that the Mo_2C MXene has strong adsorption of the hydroxyl group, with an adsorption energy of −5.31 eV. The electron DOS of spin up and down were distributed asymmetrically after the hydroxyl group was adsorbed. At the interface, the O charge of the hydroxyl group accumulates, showing a charge-rich state (yellow area). The combined Mo_2C MXene loses charge around the Mo atoms (blue area). It shows that when the hydroxyl group was adsorbed on Mo_2C MXene, it obtained electrons from Mo_2C MXene. The electron-rich hydroxyl group on the surface of the material can not only promote electron transfer between the catalyst and PMS to accelerate ROS generation, but also promote the diffusion of the catalyst in the water phase matrix. The advantage of surface hydroxyl groups in activating PMS for the degradation of toxic organic pollutants has also been explored in other studies[46]. Those properties further increase catalytic activity and enhance the mass transfer of model pollutants[7]. Those were the reason for the better repeatability of the Mo_2C MXene.

During the Mo_2C MXene/PMS cycles, the content of Mo ions in the system was also determined, with an average value of 9.7 mg L^{-1} (Supplementary Fig. 8a). It shows that Mo ions would be leached from Mo_2C MXene in the catalytic oxidation process. To further verify the contribution of leached Mo ions in BPA degradation, 10.0 mg L^{-1} Mo ions were utilized to activate PMS. The removal percentage of BPA was 20.00% within 240 min (Supplementary Fig. 8b), which indicated that the homogeneous catalysis also weakly affects the removal of BPA in the Mo_2C MXene/PMS degradation system.

Condensed Fukui function and proposed transformation pathways of BPA

To deeply analyze the transformation mechanism of BPA in the Mo_2C MXene/PMS system, we calculated the condensed Fukui function of BPA (Fig. 6a). It can predict the reaction site. The reddest atom in the figure, the larger the condensed Fukui function value f^0, the easier it is for electrophilic reactions to occur. For BPA, O1, O2, C3, C4, C6, C12, C15, and C16 are all sites with very high reactivity with $f^0 > 0.04$. The mass spectra of the possible transformation products from BPA degradation in the Mo_2C MXene/PMS system were shown in Supplementary Figs. 9–30. Figure 6b shows that BPA was first attacked by $O_2^{\bullet-}$ and $^{\bullet}OH$, which resulted in the C–C bond cleavage and hydroxylation, forming P1, then P2 generated by ring-opening[72]. Second, BPA can be oxidized by ROS to phenol (P3 and P4), then dehydrogenated and oxygenated to P6 before being hydroxylated and dehydroxylated to P7 and P9[72,73]. After BPA decomposition, C3 or/and C15 were attacked and dehydroxylated to form P5, and P6 was converted to P8 through ring-opening[3,5]. Third, BPA was oxidatively demethylated by free radicals to become P10 and P12, and P10 can also be dehydrogenated to P11. P12 transforms the hydroxylated product P13 and P14 through the electrophilic addition of $^{\bullet}OH$ to C4, C16, and C14, which was finally oxidized by $SO_4^{\bullet-}$ and $^{\bullet}OH$ to cause ring-opening and form P15. This process has also been found in other AOPs[66]. Fourth, BPA can degrade to P19 by dehydroxylation and oxidation at the C16 site and then become small molecule acids P20, P21, and P22 through C–C cleavage, $^{\bullet}OH$ addition, and elimination reactions[3]. Also, similar to the above route, BPA can convert through dehydroxylation (P17) and oxidation (P18) at C4 and C16 sites[7]. In addition, through ROS oxidation, the two methyl functional groups in the isopropyl group connecting the two phenolic rings can be transformed into alcohol and carboxyl groups (P16)[66]. Most of these intermediates were unstable and would soon be further mineralized into H_2O and CO_2. Notably, the transformation products of BPA were found to be non-toxic or low-toxic (listed in Supplementary Table 2). The acute toxicity of BPA to Mouse (intraperitoneal) and Cavia porcellus (oral) was 150.0 and 4.0 mg kg^{-1}, respectively. And the

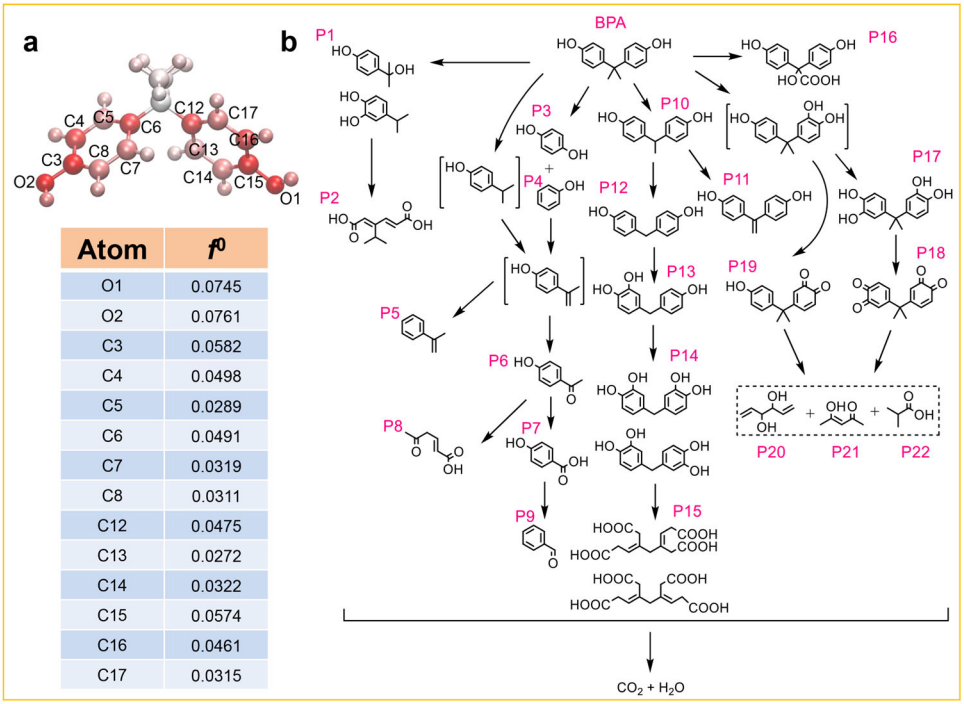

Fig. 6 The degradation and transformation mechanism of bisphenol A (BPA). a The condensed Fukui function of BPA based on density functional theory (DFT) calculation. **b** Transformation pathways for BPA in Mo_2C MXene/peroxymonosulfate (PMS) system. f^0 is the specific condensed Fukui function value.

median lethal dose (LD_{50}) of Rat (inhalation) was 17.0 mg L^{-1}. However, only the products P3, P4, P5, P6, P7, P9, P12, P20, and P22 have toxic records. Most of its toxicity values (expressed as LD_{50}) in rats (oral, inhalation, dermal) and rabbit (dermal) were as high as several hundred, or even tens of thousands of mg kg^{-1}. This implies that the transformation products of BPA after oxidation treatment by the Mo_2C MXene/PMS system were environmentally friendly.

In this work, the Mo_2C MXene with Mo-deficit vacancy defects has a good catalytic effect on PMS, producing a high reaction rate that effectively degrades BPA. It is important that the defective Mo_2C MXene has strong PMS combining and electron transfer ability. The $O_2^{\bullet-}$, $^1O_2$, $SO_4^{\bullet-}$, and $^{\bullet}OH$ generated by Mo_2C MXene activating PMS degraded BPA, and each had different contributions. The condensed Fukui function calculation was applied to predict the highly active sites in BPA and explored the possible removal pathway of BPA in the Mo_2C MXene/PMS system, according to HPLC-MS/MS analysis. This mechanism of defective Mo_2C MXene activation of PMS in BPA degradation is summarized in Fig. 7. The oxidation system constructed by Mo_2C MXene and PMS has many advantages. First, Mo_2C MXene has high adaptability for persulfate-based oxidants (including PMS and PS). Second, the Mo_2C MXene/PMS system could oxidatively degrade various pollutants, including bisphenol endocrine disruptors, polycyclic aromatic hydrocarbon persistent pollutants, and plasticizers. Third, compared with some catalysts, the applicable pH range of Mo_2C MXene/PMS system was wider, and the degradation percentage of BPA was above 74% under all pH conditions. Fourth, some hydroxyl groups would be loaded on the surface when Mo_2C MXene participated in the activation of PMS, which improved the repeatability of Mo_2C MXene. Furthermore, the transformation product of BPA was environmentally friendly and would not harm the ecological environment. Therefore, the Mo_2C MXene/PMS system was suitable for BPA degradation in actual water, and the degradation percentage remained high.

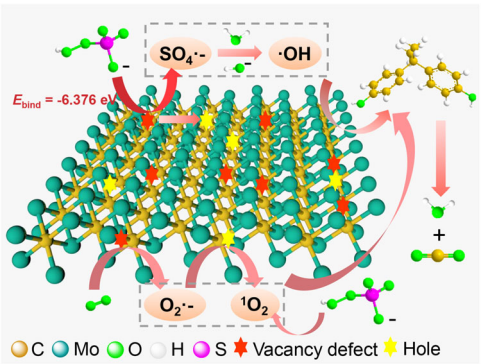

Fig. 7 The degradation mechanism. Proposed mechanism of Mo_2C MXene activating peroxymonosulfate (PMS) for the degradation of bisphenol A (BPA).

METHODS

Materials

Bisphenol A (BPA, $C_{15}H_{16}O_2$, >99.0%), Peroxymonosulfate (PMS, $2KHSO_5{\cdot}KHSO_4{\cdot}K_2SO_4$, PMS) were provided by Sigma-Aldrich (Saint Louis, MO, USA); 2,2,6,6-tetramethylpiperidine (TEMP, ≥98.0%) was obtained from Dojindo (Kumamoto, Japan); 5,5-Dimethyl-1-pyrroline N-oxide (DMPO, 98.0%) was purchased from J&K Scientific (Shanghai, China); and Mo_2Ga_2C were provided by Yiyi Technology Co., Ltd. (Jilin, China). Other related chemicals used were reagent grade, while deionized water was obtained from an ultrapure water system.

Catalytic activity measurement

The chemical experiments reacted in 20 mL glass bottles. First, 9.5 mL of the prepared 2 mg L^{-1} BPA was put into the reaction flask, then 10 mg Mo_2C MXene was weighed into the system, before finally adding 0.5 mL of 40 mmol L^{-1} PMS to trigger the

experiment. The dosage of Mo_2C MXene was 0.5 g L^{-1}, and PMS was 2 mmol L^{-1} in the system. And using 1 mol L^{-1} H_2SO_4 and NaOH to adjust the solution pH (3–10). The batch experiment was under a constant temperature oscillator at 25 °C and protected from light. At the specific time point, 0.5 mL of methanol was used to quench an equal amount of the reaction solution, then filter the mixture of methanol and reaction solution using an organic filter (0.22 μm). And the HPLC (Shimadzu DGU-20A_5, Japan) with an inertsil C18 column was used to analyze the residual BPA content. The experiments were done in triplicates for comparison, and the correlation is accepted at $p < 0.05$.

Characterization of Mo_2C MXene

The phase analysis of Mo_2Ga_2C and Mo_2C MXene was done using X-ray diffraction (XRD, X'TRA, Thermo Fisher Scientific, USA) at a Cu-Ka X-ray source with 40 kV pipe pressure and 40 mA pipe flow. The surface morphology was analyzed using a field emission scanning electron microscope (SEM; Zeiss HD, Germany) and a transmission electron microscope (TEM; JEOL JEM 2100F, Japan). And the surface element state determination was done using an X-ray photoelectron spectrometer (XPS, Axis Ultra DLD Kratos AXIS SUPRA, Japan) equipped at an Al-Ka source, and calibrated by C–C (284.8), while the surface functional group analysis was a Fourier transform infrared spectroscopy (FTIR, Bruker Vertex 70, Germany) on KBr tablets and the surface vacancy defects were measured by electron paramagnetic resonance (EPR, E500-9.5/12, Bruker, Germany). The total concentration of leached Mo was analyzed by inductively coupled plasma-optical emission spectroscopy (Optima 5300DV, Perkin Elmer, USA). The degradation efficiency calculation equation and pseudo-first-order kinetics model were shown in Supplementary Methods.

Cyclic voltammograms (CV) and electrochemical impedance spectroscopy (EIS) tests

The electrochemical workstation was utilized to investigate the cyclic voltammograms (CV) and electrochemical impedance spectroscopy (EIS). The experiments include glassy carbon, Ag/AgCl, and platinum electrode. And KOH with 0.1 mol L^{-1} was chosen as the electrolyte. Moreover, the sweep speed was 50 mV s^{-1}, and the CV sweep range was −1.0 to 0.5 V. The EIS was tested under open circuit potential (frequency: 1 MHz–0.1 Hz, amplitude: 5 mV AC).

Electron paramagnetic resonance test

EPR was used to determine ROS: $SO_4^{\bullet-}$, $^{\bullet}OH$, and $^1O_2$ were measured in the water phase, while $O_2^{\bullet-}$ was measured in the DMSO phase. $SO_4^{\bullet-}$, $^{\bullet}OH$, and $O_2^{\bullet-}$ were captured by 100 mmol L^{-1} of DMPO, while $^1O_2$ was captured by 30 mmol L^{-1} of TEMP. The degradation products of BPA were analyzed by a high-performance liquid chromatography-mass spectrometer (HPLC-MS), and the MS was electrospray ionization mass spectrometry (Thermo Fisher, USA). The full scan spectrum was measured in the positive ion mode in the m/z 50–1000 scan range, using high-purity nitrogen as the atomizer and drying gas.

Computational chemical analysis

The binding energies are calculated based on density functional theory (DFT), which utilizes the VASP[74,75] with the frozen-core all-electron PAW[76,77]. The Perdew–Burke–Ernzerhof[78] of generalized gradient approximation was used to explain the exchange and correlation potential. A monolayer 4 × 4 defective Mo_2C/undefective Mo_2C (001) supercell was used. The HSO_5^- molecule was placed on the top-site of Mo in Mo_2C MXene, and a 20 Å vacuum area was added to decrease the interaction. Perform geometric optimization until the force on each ion drops below 0.01 eV/Å. The Monkhorst-Pack k-point sampling was set to 2 × 2 × 1[79]. The binding energy (E_{bind}) is calculated using the Eq. 12.

$$E_{bind} = E_{molecule+surface} - (E_{surface} + E_{molecule}) \quad (12)$$

where $E_{surface}$ is the energy of defective Mo_2C/undefective Mo_2C (001) supercell, $E_{molecule}$ represents the energy of HSO_5^-, $E_{molecule\ +\ surface}$ represents the total energy.

The calculation method of the DOS is shown in Supplementary Methods. The condensed Fukui function was calculated through computational chemistry optimization. Firstly, Chemoffice 19 software was used to draw the molecular structure of BPA, and then Gaussian 09 W software was utilized to optimize the molecule by the DFT at the ωB97XD/6-31G basis set. Finally, Multiwfn 3.8 was used in the calculations before displaying using VMD[80].

DATA AVAILABILITY

The authors declare that the data supporting the findings of this study are available within the paper (and its Supplementary information files).

Received: 8 July 2022; Accepted: 15 December 2022;
Published online: 26 December 2022

REFERENCES

1. Bittner, G. D., Yang, C. Z. & Stoner, M. A. Estrogenic chemicals often leach from BPA-free plastic products that are replacements for BPA-containing polycarbonate products. *Environ. Health* **13**, 41 (2014).
2. Schecter, A. et al. Bisphenol A (BPA) in U.S. Food. *Environ. Sci. Technol.* **44**, 9425–9430 (2010).
3. Wang, F. et al. Facile fabricate of novel Co(OH)F@MXenes catalysts and their catalytic activity on bisphenol A by peroxymonosulfate activation: the reaction kinetics and mechanism. *Appl. Catal. B* **262**, 118099 (2020).
4. Li, X. et al. Long-term exposure to bisphenol A and its analogues alters the behavior of marine medaka (*Oryzias melastigma*) and causes hepatic injury. *Sci. Total Environ.* **841**, 156590 (2022).
5. Abdelraheem, W. H. M., Patil, M. K., Nadagouda, M. N. & Dionysiou, D. D. Hydrothermal synthesis of photoactive nitrogen- and boron- codoped TiO_2 nanoparticles for the treatment of bisphenol A in wastewater: synthesis, photocatalytic activity, degradation byproducts and reaction pathways. *Appl. Catal. B* **241**, 598–611 (2019).
6. Idowu, G. A., David, T. L. & Idowu, A. M. Polycarbonate plastic monomer (bisphenol-A) as emerging contaminant in Nigeria: levels in selected rivers, sediments, well waters and dumpsites. *Mar. Pollut. Bull.* **176**, 113444 (2022).
7. Dong, X. et al. Monodispersed $CuFe_2O_4$ nanoparticles anchored on natural kaolinite as highly efficient peroxymonosulfate catalyst for bisphenol A degradation. *Appl. Catal. B* **253**, 206–217 (2019).
8. Zhang, Y. et al. Polypyrrole/reduced graphene oxide aerogel particle electrodes for high-efficiency electro-catalytic synergistic removal of Cr(VI) and bisphenol A. *Chem. Eng. J.* **336**, 690–700 (2018).
9. Rajabnejad, S.-H. et al. Aptasensors as promising new tools in bisphenol A detection —an invisible pollution in food and environment. *Microchem. J.* **155**, 104722 (2020).
10. Ju, L., Wu, P., Yang, Q., Ahmed, Z. & Zhu, N. Synthesis of ZnAlTi-LDO supported C_{60}@AgCl nanoparticles and their photocatalytic activity for photo-degradation of Bisphenol A. *Appl. Catal. B* **224**, 159–174 (2018).
11. Jia, J. et al. Comparative study on bisphenols oxidation via TiO_2 photocatalytic activation of peroxymonosulfate: effectiveness, mechanism and pathways. *J. Hazard. Mater.* **424**, 127434 (2022).
12. Zhang, X. et al. Enhanced visible-light-assisted peroxymonosulfate activation over $MnFe_2O_4$ modified g-C_3N_4/diatomite composite for bisphenol A degradation. *Int. J. Min. Sci. Techno.* **31**, 1169–1179 (2021).
13. Liu, C. et al. Coupling metal-organic frameworks and g-C_3N_4 to derive Fe@N-doped graphene-like carbon for peroxymonosulfate activation: upgrading framework stability and performance. *Appl. Catal. B* **255**, 117763 (2019).
14. Ozyildiz, G., Olmez-Hanci, T. & Arslan-Alaton, I. Effect of nano-scale, reduced graphene oxide on the degradation of bisphenol A in real tertiary treated wastewater with the persulfate/UV-C process. *Appl. Catal. B* **254**, 135–144 (2019).
15. Guo, S. et al. Scalable synthesis of Ca-doped α-Fe_2O_3 with abundant oxygen vacancies for enhanced degradation of organic pollutants through peroxymonosulfate activation. *Appl. Catal. B* **262**, 118250 (2020).
16. Ghanbari, F. & Moradi, M. Application of peroxymonosulfate and its activation methods for degradation of environmental organic pollutants: review. *Chem. Eng. J.* **310**, 41–62 (2017).

17. Forouzesh, M., Ebadi, A. & Aghaeinejad-Meybodi, A. Degradation of metronidazole antibiotic in aqueous medium using activated carbon as a persulfate activator. *Sep. Purif. Technol.* **210**, 145–151 (2019).
18. Mora, V. C., Rossoa, J. A., Carrillo Le Roux, G., Martire, D. O. & Gonzalez, M. C. Thermally activated peroxydisulfate in the presence of additives: a clean method for the degradation of pollutants. *Chemosphere* **75**, 1405–1409 (2009).
19. Furman, O. S., Teel, A. L. & Watts, R. J. Mechanism of base activation of persulfate. *Environ. Sci. Technol.* **44**, 6423–6428 (2010).
20. Anipsitakis, G. P. & Dionysiou, D. D. Degradation of organic contaminants in water with sulfate radicals generated by the conjunction of peroxymonosulfate with cobalt. *Environ. Sci. Technol.* **37**, 4790–4797 (2003).
21. Bensaid, S. et al. A simple model for a complex system: Kinetics of water oxidation with the $[Ru(bpy)_3]^{2+}/S_2O_8^{2-}$ photosystem as catalyzed by Mn_2O_3 under different illumination conditions. *Chem. Eng. J.* **311**, 143–152 (2017).
22. Nfodzo, P. & Choi, H. Triclosan decomposition by sulfate radicals: effects of oxidant and metal doses. *Chem. Eng. J.* **174**, 629–634 (2011).
23. Naguib, M. et al. Two-dimensional nanocrystals produced by exfoliation of Ti_3AlC_2. *Adv. Mater.* **23**, 4248–4253 (2011).
24. Barsoum, M. W. The $M_{N+1}AX_N$ phases: a new class of solids. *Prog. Solid. State Chem.* **28**, 201–281 (2000).
25. Tan, C. et al. Recent advances in ultrathin two-dimensional nanomaterials. *Chem. Rev.* **117**, 6225–6331 (2017).
26. Li, D. et al. Noble-metal-free Mo_2C co-catalsyt modified perovskite oxide nanosheet photocatalysts with enhanced hydrogen evolution performance. *Colloid Surf. A* **615**, 126252 (2021).
27. Liu, Y. et al. Regulating electron–hole separation to promote photocatalytic H_2 evolution activity of nanoconfined Ru/MXene/TiO_2 catalysts. *ACS Nano* **14**, 14181–14189 (2020).
28. Liu, X. et al. Metal-organic framework nanocrystal-derived hollow porous materials: synthetic strategies and emerging applications. *Innovation* **3**, 100281 (2022).
29. Zhang, Y. et al. Application of MOFs and COFs for photocatalysis in CO_2 reduction, H_2 generation, and environmental treatment. *EnergyChem* **4**, 100078 (2022).
30. Yu, S. et al. MXenes as emerging nanomaterials in water purification and environmental remediation. *Sci. Total Environ.* **811**, 152280 (2022).
31. Shi, Z. et al. Phosphorus-Mo_2C@carbon nanowires toward efficient electrochemical hydrogen evolution: composition, structural and electronic regulation. *Energy Environ. Sci.* **10**, 1262–1271 (2017).
32. Kou, Z. et al. Rational design of holey 2D nonlayered transition metal carbide/nitride heterostructure nanosheets for highly efficient water oxidation. *Adv. Energy Mater.* **9**, 1803768 (2019).
33. Sang, X. et al. Atomic defects in monolayer titanium carbide ($Ti_3C_2T_x$) MXene. *ACS Nano* **10**, 9193–9200 (2016).
34. Wu, H., Guo, Z., Zhou, J. & Sun, Z. Vacancy-mediated lithium adsorption and diffusion on MXene. *Appl. Surf. Sci.* **488**, 578–585 (2019).
35. Liu, Y. et al. A modulated electronic state strategy designed to integrate active HER and OER components as hybrid heterostructures for efficient overall water splitting. *Appl. Catal. B* **260**, 118197 (2020).
36. Wang, W. et al. The confined interlayer growth of ultrathin two-dimensional Fe_3O_4 nanosheets with enriched oxygen vacancies for peroxymonosulfate activation. *Acs. Catal.* **11**, 11256–11265 (2021).
37. Zhu, C. et al. Confinement of CoP nanoparticles in nitrogen-doped yolk-shell porous carbon polyhedron for ultrafast catalytic oxidation. *Adv. Funct. Mater.* **30**, 2003947 (2020).
38. Zhang, W., Yan, X., Liu, Z. & Du, C. Halloysite nanotubes supported copper oxide composites used as efficient catalysts for bisphenol A removal. *Appl. Clay Sci.* **224**, 106509 (2022).
39. Chen, H., Motuzas, J., Martens, W. & Diniz da Costa, J. C. Surface and catalytic properties of stable Me(Ba, Ca and Mg)SrCoO for the degradation of orange II dye under dark conditions. *Appl. Surf. Sci.* **450**, 292–300 (2018).
40. Sun, H., Yang, X., Zhao, L., Xu, T. & Lian, J. One-pot hydrothermal synthesis of octahedral CoFe/$CoFe_2O_4$ submicron composite as heterogeneous catalysts with enhanced peroxymonosulfate activity. *J. Mater. Chem. A* **4**, 9455–9465 (2016).
41. Zheng, H. et al. Efficient degradation of atrazine with porous sulfurized Fe_2O_3 as catalyst for peroxymonosulfate activation. *Appl. Catal. B* **259**, 118056 (2019).
42. Tang, L. et al. Enhanced activation process of persulfate by mesoporous carbon for degradation of aqueous organic pollutants: electron transfer mechanism. *Appl. Catal. B* **231**, 1–10 (2018).
43. Duan, X. et al. Surface controlled generation of reactive radicals from persulfate by carbocatalysis on nanodiamonds. *Appl. Catal. B* **194**, 7–15 (2016).
44. Yu, C. et al. Development of a novel biochar/iron oxide composite from green algae for bisphenol-A removal: adsorption and Fenton-like reaction. *Environ. Technol. Innov.* **28**, 102647 (2022).
45. Chen, X. et al. Ce(III) activates peroxymonosulfate for the degradation of substituted PAHs. *Chemosphere* **306**, 135525 (2022).
46. Zhong, Q. et al. Efficient degradation of organic pollutants by activated peroxymonosulfate over TiO_2@C decorated Mg-Fe layered double oxides: degradation pathways and mechanism. *Chemosphere* **300**, 134564 (2022).
47. Grebel, J. E., Pignatello, J. J. & Mitch, W. A. Effect of halide ions and carbonates on organic contaminant degradation by hydroxyl radical-based advanced oxidation processes in saline waters. *Environ. Sci. Technol.* **44**, 6822–6828 (2010).
48. Cai, S. et al. Pyrrolic N-rich biochar without exogenous nitrogen doping as a functional material for bisphenol A removal: performance and mechanism. *Appl. Catal. B* **291**, 120093 (2021).
49. Abbas, W. et al. Development of polystyrene coated persulfate slow-release beads for the oxidation of targeted PAHs: effects of sulfate and chloride ions. *J. Hazard. Mater.* **416**, 125879 (2021).
50. Huang, Y. et al. Degrading arsanilic acid and adsorbing the released inorganic arsenic simultaneously in aqueous media with $CuFe_2O_4$ activating peroxymonosulfate system: factors, performance, and mechanism. *Chem. Eng. J.* **424**, 128537 (2021).
51. Anipsitakis, G. P., Dionysiou, D. D. & Gonzalez, M. A. Cobalt-mediated activation of peroxymonosulfate and sulfate radical attack on phenolic compounds. Implications of chloride ions. *Environ. Sci. Technol.* **40**, 1000–1007 (2006).
52. Li, J., Wan, Y., Li, Y., Yao, G. & Lai, B. Surface Fe(III)/Fe(II) cycle promoted the degradation of atrazine by peroxymonosulfate activation in the presence of hydroxylamine. *Appl. Catal. B* **256**, 117782 (2019).
53. Tan, W. et al. Removal of levofloxacin through adsorption and peroxymonosulfate activation using carbothermal reduction synthesized nZVI/carbon fiber. *Chemosphere* **280**, 130626 (2021).
54. Yuan, R., Ramjaun, S. N., Wang, Z. & Liu, J. Effects of chloride ion on degradation of Acid Orange 7 by sulfate radical-based advanced oxidation process: Implications for formation of chlorinated aromatic compounds. *J. Hazard. Mater.* **196**, 173–179 (2011).
55. Khajeh, M., Amin, M. M., Fatehizadeh, A. & Aminabhavi, T. M. Synergetic degradation of atenolol by hydrodynamic cavitation coupled with sodium persulfate as zero-waste discharge process: effect of coexisting anions. *Chem. Eng. J.* **416**, 129163 (2021).
56. Hammad, M. et al. Enhanced heterogeneous activation of peroxymonosulfate by Ruddlesden-Popper-type $La_2CoO_{4+\delta}$ nanoparticles for bisphenol A degradation. *Chem. Eng. J.* **429**, 131447 (2021).
57. Zhong, Q., Liu, J., Wang, Z., Ghasemi, J. B. & Zhang, G. Ti_3C_2 MXene/Ag_2ZnGeO_4 Schottky heterojunctions with enhanced photocatalytic performances: efficient charge separation and mechanism studies. *Sep. Purif. Technol.* **278**, 119560 (2022).
58. Liu, H. et al. Oxidation of benzene by persulfate in the presence of Fe(III)- and Mn(IV)-containing oxides: stoichiometric efficiency and transformation products. *Environ. Sci. Technol.* **50**, 890–898 (2016).
59. Pan, L., Shi, W., Sen, T., Wang, L. & Zhang, J. Visible light-driven selective organic degradation by $FeTiO_3$/persulfate system: the formation and effect of high valent Fe(IV). *Appl. Catal. B* **280**, 119414 (2021).
60. Guo, T. et al. Efficient persulfate activation by hematite nanocrystals for degradation of organic pollutants under visible light irradiation: facet-dependent catalytic performance and degradation mechanism. *Appl. Catal. B* **286**, 119883 (2021).
61. Li, B. et al. Unravelling the interfacial charge migration pathway at atomic level in 2D/2D interfacial Schottky heterojunction for visible-light-driven molecular oxygen activation. *Appl. Catal. B* **266**, 118650 (2020).
62. Zhong, Q., Li, Y., Zhang, G. & Zhang, G. Two-dimensional MXene-based and MXene-derived photocatalysts: recent developments and perspectives. *Chem. Eng. J.* **409**, 128099 (2021).
63. Zhou, Y., Niu, J., Zhang, G., Yu, M. & Yang, F. A three-dimensional self-standing Mo_2C/nitrogen-doped graphene aerogel: Enhancement hydrogen production from landfill leachate wastewater in MFCs-AEC coupled system. *Environ. Res.* **184**, 109283 (2020).
64. Jia, S., Wang, Q., Chen, J. & Wang, S. High-active nanoplates of nitrogen-doped carbon@Mo_2C as efficient catalysts in water splitting. *Synth. Metals* **279**, 116847 (2021).
65. Sun, M. et al. Mg doped CuO–Fe_2O_3 composites activated by persulfate as highly active heterogeneous catalysts for the degradation of organic pollutants. *J. Alloy. Compd.* **825**, 154036 (2020).
66. Chen, H., Xu, Y., Zhu, K. & Zhang, H. Understanding oxygen-deficient $La_2CuO_{4-\delta}$ perovskite activated peroxymonosulfate for bisphenol A degradation: The role of localized electron within oxygen vacancy. *Appl. Catal. B* **284**, 119732 (2021).
67. Li, G. et al. N-doped Mo_2C nanobelts/graphene nanosheets bonded with hydroxy nanocellulose as flexible and editable electrode for hydrogen evolution reaction. *iScience* **19**, 1090–1100 (2019).
68. Song, H. et al. Anchoring single atom cobalt on two-dimensional MXene for activation of peroxymonosulfate. *Appl. Catal. B* **286**, 119898 (2021).

69. Tang, X. et al. MXene-based dendrite-free potassium metal batteries. *Adv. Mater.* **32**, 1906739 (2020).
70. Zhao, D. et al. MXene (Ti_3C_2) vacancy-confined single-atom catalyst for efficient functionalization of CO_2. *J. Am. Chem. Soc.* **141**, 4086–4093 (2019).
71. Gong, S. et al. Visible light-driven, selective CO_2 reduction in water by in-doped Mo_2C based on defect engineering. *Appl. Catal. B* **310**, 121333 (2022).
72. Ji, Q. et al. Visible light absorption by perylene diimide for synergistic persulfate activation towards efficient photodegradation of bisphenol A. *Appl. Catal. B* **282**, 119579 (2021).
73. Rodríguez, E. M. et al. Efficiency of different solar advanced oxidation processes on the oxidation of bisphenol A in water. *Appl. Catal. B* **95**, 228–237 (2010).
74. Kresse, G. & Hafner, J. Ab initio molecular-dynamics simulation of the liquid-metal-amorphous-semiconductor transition in germanium. *Phys. Rev. B* **49**, 14251–14269 (1994).
75. Kresse, G. & Furthmüller, J. Efficient iterative schemes for ab initio total-energy calculations using a plane-wave basis set. *Phys. Rev. B* **54**, 11169–11186 (1996).
76. Blöchl, P. E. Projector augmented-wave method. *Phys. Rev. B* **50**, 17953–17979 (1994).
77. Kresse, G. & Joubert, D. From ultrasoft pseudopotentials to the projector augmented-wave method. *Phys. Rev. B* **59**, 1758–1775 (1999).
78. Hammer, B., Hansen, L. B. & Nørskov, J. K. Improved adsorption energetics within density-functional theory using revised Perdew–Burke–Ernzerhof functionals. *Phys. Rev. B* **59**, 7413–7421 (1999).
79. Monkhorst, H. J. & Pack, J. D. Special points for Brillouin-zone integrations. *Phys. Rev. B* **13**, 5188–5192 (1976).
80. Lu, T. & Chen, F. Multiwfn: a multifunctional wavefunction analyzer. *J. Comput. Chem.* **33**, 580–592 (2012).

ACKNOWLEDGEMENTS

This work was financially supported by the National Science Foundation of China (41877125, 22161132011, and 41925029), National Key R&D Plan Key Projects (2021YFC1809100), and Jiangsu Provincial Science and Technology Innovation Fund for Carbon Dioxide Emission Peak and Carbon Neutrality (20220013).

AUTHOR CONTRIBUTIONS

X.C.: Conceptualization, methodology, investigation, and writing-original draft. F.O.G.: Investigation, writing-review & editing, language improvement. X.Hu: Methodology. M.G.W.: Writing-review & editing, language improvement. Y.G.: Resources, supervision, conceptualization, writing-review & editing. All the authors have read and approved the paper.

COMPETING INTERESTS

The authors declare no competing interests.

ADDITIONAL INFORMATION

Supplementary information The online version contains supplementary material available at https://doi.org/10.1038/s41545-022-00214-w.

Correspondence and requests for materials should be addressed to Yanzheng Gao.

Reprints and permission information is available at http://www.nature.com/reprints

Publisher's note Springer Nature remains neutral with regard to jurisdictional claims in published maps and institutional affiliations.

Open Access This article is licensed under a Creative Commons Attribution 4.0 International License, which permits use, sharing, adaptation, distribution and reproduction in any medium or format, as long as you give appropriate credit to the original author(s) and the source, provide a link to the Creative Commons license, and indicate if changes were made. The images or other third party material in this article are included in the article's Creative Commons license, unless indicated otherwise in a credit line to the material. If material is not included in the article's Creative Commons license and your intended use is not permitted by statutory regulation or exceeds the permitted use, you will need to obtain permission directly from the copyright holder. To view a copy of this license, visit http://creativecommons.org/licenses/by/4.0/.

© The Author(s) 2022